Circumventing Metal Dissolution Induced Degradation of Pt-Alloy Catalysts in Proton Exchange Membrane Fuel Cells: Revealing the Asymmetric Volcano Nature of Redox Catalysis

Qingying Jia,[†] Jingkun Li,[†] Keegan Caldwell,[‡] David E. Ramaker,[‡] Joseph M. Ziegelbauer,[§] Ratandeep S. Kukreja,[§] Anusorn Kongkanand,[∥] and Sanjeev Mukerjee*,[†]

[†]Department of Chemistry & Chemical Biology, Northeastern University, Boston, Massachusetts 02115, United States
[‡]Department of Chemistry, George Washington University, Washington, D.C. 20052, United States
[§]Global Fuel Cell Activities, General Motors Central Research & Development, Warren, Michigan 48090, United States
[∥]Global Fuel Cell Activities, General Motors Global Powertrain, Pontiac, Michigan 48340, United States

Ⓢ *Supporting Information*

ABSTRACT: One of the major obstacles to the commercialization of proton exchange membrane fuel cells (PEMFCs) is the usage of scarce platinum in the cathode for the oxygen reduction reaction (ORR). Although progress has been made in reducing Pt usage by alloying with transition metals M (M = Co, Ni, Cu, etc.), practical applications of Pt-M/C catalysts are impeded by their insufficient durability under the highly corrosive conditions at a PEMFC cathode. Herein, we reconcile the durability difficulty by demonstrating that the high mass activity of the dealloyed $PtNi_3/C$ catalyst with low nanoporosity further increases after 30k voltage cycles in PEMFCs. A novel method has been developed to implement an in situ X-ray absorption spectroscopy study of these PEMFC-cycled catalysts under operating conditions to understand the unusual activity trend. We reveal that the ORR activity of $PtNi_3/C$ catalysts with varied nanoporosities exhibits a Sabatier volcano curve as a function of the strain governed by Ni content, and the volcano is skewed toward the Pt−O weak binding leg owing to the asymmetric site-blocking effect. The Ni dissolution during PEMFC operation, which was previously believed to be detrimental, becomes beneficial for the solid $PtNi_3/C$ catalysts located on the Pt−O weak binding leg because it leads to the activity ascending toward the apex, and meanwhile the activity remains high throughout the long-term operation owing to the minimal site-blocking effect. More generally, the fundamental insights into the universal asymmetric volcano curve of redox catalysis will potentially guide the rational design of a broad variety of catalytic materials.

KEYWORDS: fuel cell degradation, oxygen reduction reaction, durability, strain effects, site-blocking effect
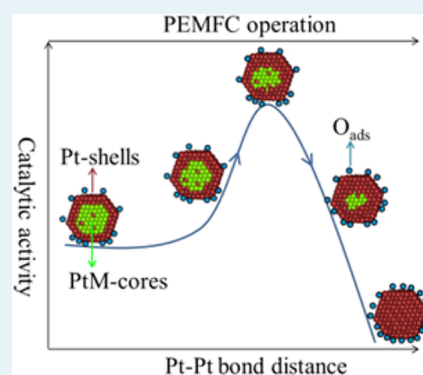
1. INTRODUCTION

Proton exchange membrane fuel cells (PEMFCs) are promising alternatives to the internal combustion engine using fossil fuels owing to their high energy efficiency and zero emissions.[1,2] However, large-scale applications of PEMFCs are limited by the high Pt loading required at the cathodes in order to efficiently catalyze the oxygen reduction reaction (ORR).[3,4] Pt-based alloys have gained considerable attention in the past decades owing to their improved ORR activity in comparison to pure Pt catalysts.[4−10] A promising class of highly active catalysts in PEMFCs are the (electro)chemically dealloyed PtM_x/C (where M = Co, Ni, Cu, etc.) nanoparticle (NP) catalysts with initially high M content ($x > 1$) in the precursors; they exhibit approximately 4−8 times higher Pt mass activity (MA; A mg_{Pt}^{-1} @ 0.9 V vs reversible hydrogen electrode) and 4−7 times higher specific activities (SA; μA $cm_{Pt,REAL}^{-2}$ @ 0.9 V) toward the ORR over state-of-the-art Pt/C catalysts in membrane-electrode-assembly (MEA) evaluations.[11−13] How-

ever, the practical applications of these catalysts are hindered by their poor durability over long-term operation in PEMFCs.[12,14] While durable Pt-based catalysts for PEMFCs have been produced by alloying Pt with less soluble elements such as Pd and Au,[15,16] these catalysts display inferior ORR activities to dealloyed PtM_x/C NPs. Guided by Nørskov et al.'s computational screening of a broad variety of binary alloys,[17] Chorkendorff's group recently discovered a new class of catalysts by alloying Pt with rare-earth metals such as Y, La, Gd, etc.[18,19] These Pt−rare-earth alloys demonstrated high ORR activity and durability in rotating disk electrode (RDE) measurements.[18,19] Despite these advances, further improvements of both the activity and durability of Pt-based electrocatalysts in real PEMFCs are essential for viability. A

potentially feasible pathway for the design of such catalysts is to significantly improve the durability of dealloyed PtM$_x$/C catalysts without compromising their activity.

The enhanced ORR activity of dealloyed PtM$_x$/C catalysts over Pt/C originates primarily from the surface strain induced by the lattice mismatch between the Pt-rich outer shell and M-rich core and its concomitant electronic effects.[20,21] Correspondingly, the poor durability of these catalysts arises from the dissolution of the more soluble M during operation in acidic environments, resulting in concomitant particle growth via a dissolution and precipitation mechanism.[22−26] Extensive research efforts have focused on suppressing the acidic dissolution of M to improve the durability.[12,13,22,23,27] Recently, Strasser et al.[23] reported that solid dealloyed PtNi$_x$/C NPs with low nanoporosity exhibit superior ORR durability to porous analogues because the Ni is better protected by the Pt shells against dissolution. However, M dissolution has always been related to activity loss thus far, which limits the room for further durability improvements.

From a fundamental point of view, M dissolution from PtM$_x$/C NPs is not necessarily bound to ORR activity loss. According to the d-band theory developed by Nørskov et al.,[28−30] strain and/or ligand effects induced by M can modify the Pt−O bond strength via shifting the Pt d-band relative to the Fermi level. The ORR rate tracks with this change following a Sabatier volcano-type behavior (Scheme 1). Pure Pt is located

Scheme 1. Sabatier Volcano-Type Behavior of the Catalytic Activity of PtM$_x$ Catalysts as a Function of Pt−O Binding Energy
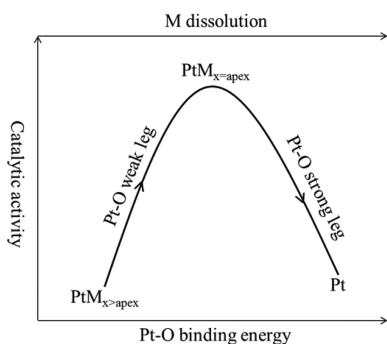
on the strong binding leg of the volcano, as the Pt−O bond strength is too strong. As a result, the ORR rate is limited by the removal of poisonous O and/or OH species (denoted as O(H)* hereafter). The strain/ligand effects shift the activity up via weakening of the Pt−O bond strength until an optimal Pt−O binding energy is reached (e.g., the apex of the volcano). Accordingly, the strain/ligand attenuation induced by M dissolution downshifts the activity away from the apex along the strong binding leg, which is commonly acknowledged as the dominant factor for the degradation of PtM$_x$/C catalysts during PEMFC operation.[11,21,24,31,32] If the Pt−O binding energy is overly weakened by excessive M in PtM$_x$/C NPs, the activity is expected to be located on the weak binding leg of the volcano curve, and the ORR rate is limited by the dissociation of adsorbed O$_2$ associated with charge transfer. Accordingly, the M dissolution with consequent strain attenuation upshifts the activity along the Pt−O weak binding leg until reaching the apex (Scheme 1). In addition to the reaction kinetics, it has been pointed out that the site-blocking effect induced by the accumulation of oxygen adsorbates on a Pt surface may play a

dominant role for the ORR activity of Pt-based catalysts and therefore must be considered for a proper understanding of the ORR mechanisms.[33]

Despite the theoretical possibility of M dissolution increasing the ORR activity of PtM$_x$/C catalysts, such a phenomenon has never been verified experimentally, owing to the synthesis and characterization difficulties.[24] To remain on the Pt−O weak binding leg of the volcano curve, the PtM$_x$/C NPs need to retain high M content at the beginning-of-life (BOL) stage in PEMFCs after extensive acidic pretreatment, as well as the end-of-life (EOL) stage upon sufficiently long or severe cycling in PEMFCs. However, the M content in previous dealloyed PtM$_x$/C catalysts subjected to acidic pretreatment appears to saturate around 25% irrespective of the initial composition, as the loss of M during dealloying increases drastically with increasing initial M content in the precursor.[21,34] The majority of the residual M atoms are further leached out during PEMFC operation, and usually only trace amounts of M are found in these catalysts at the end of long-term operation. Consequently, the ORR activities at the EOL are comparable to those of pure Pt/C with similar particle sizes.[13,24,32] In addition to the synthetic challenges, the experimental verification of the Sabatier principle, i.e. observation of molecular oxygenated adsorbates (HOOH and/or OOH denoted as (H)OOH*) on the Pt−O weak leg and atomic oxygenated adsorbates (O(H)*) on the Pt−O strong leg of the volcano curve, has been elusive as summarized in our previous work,[31] but we were able to discern that the adsorption of (H)OOH* and O(H)* could be differentiated using advanced surface-sensitive $\Delta\mu$ analysis. This analytical procedure was able to provide confirmation of the Sabatier principle.[35]

By employing synchrotron-based in situ X-ray absorption spectroscopy (XAS) on several fresh PtCo$_x$/C catalysts with various Pt/Co atomic ratios, we observed that the ORR specific activity follows a liner relationship with both the bulk average Pt−Pt bond distance (R_{PtPt}) and Co content.[21] This linear correlation follows the descending side of the Sabatier volcano curve. However, our efforts to characterize the PtCo$_x$/C catalysts cycled in PEMFCs by in situ XAS were impeded by the convolution of the Pt and Co signal arising from those elements existing in both the electrode and the membrane.[24] This is because the catalyst(s) in these MEAs fabricated by a catalyst-coated membrane (CCM) essentially became a physically intimate part of the membrane after hot-pressing, and both Pt and Co migrate into the membrane during PEMFC operation.[24,32] This issue is addressed here by employing a technique for fabricating an MEA with a catalyst-coated diffusion media (CCDM) cathode.[36] While the CCDM anodes were hot-pressed into the membrane, the cathode CCDMs were not hot-pressed but merely physically laid upon the surface of the membrane. The only pressing which they received was from the torquing down of the cell hardware. This novel method ensures that the majority of the cathode catalyst remains on the gas diffusion later (GDL) after detachment from the membrane post MEA testing. This isolated electrode was then transferred into a previously described in situ spectroelectrochemical half-cell[37] for the in situ XAS measurements. For the first time, the Pt−M/C catalysts cycled in real PEMFCs are characterized by in situ XAS to capture the local structural evolution upon PEMFC operation, which provides unique insights into the degradation mechanisms of Pt−M/C catalysts. Moreover, we have recently reported that it is possible to directly identify the molecular adsorbates on the surfaces of

PtM$_x$/C catalysts by employing the surface-sensitive $\Delta\mu$-XANES (X-ray absorption near edge spectroscopy) technique.[31] These recent advances in XAS analysis make it a suitable technique to address the characterization difficulties mentioned above. The synthesis difficulties are also addressed here by reducing the nanoporosity of PtNi$_3$/C catalysts. Among the four PtNi$_3$/C catalysts studied here, the one with the lowest nanoporosity contains ~35.7 atom % Ni after acid pretreatment, far exceeding the saturation value (~25%) found on previously reported dealloyed PtM$_x$/C catalysts.

In the present work, we have systematically investigated the changes in composition, structure, and activity of a series of dealloyed PtNi$_3$/C catalysts with manipulated nanoporosity during PEMFC operation by employing in situ XAS in conjunction with ex situ microscopic characterization techniques. We show that the mass activity of a dealloyed PtNi$_3$/C catalyst with ultralow nanoporosity increases after 30k voltage cycles in a PEMFC despite substantial Ni dissolution. This verifies that the M dissolution is not doomed as a detrimental effect on ORR activity, thereby eliminating the degradation of dealloyed Pt−M/C catalysts induced by the inevitable M dissolution during PEMFC operation up to 30k cycles. In addition to the practical achievements, we experimentally confirm an asymmetric Sabatier volcano-type behavior of the specific activity of the dealloyed PtNi$_3$/C catalysts and show that the M dissolution during MEA operation can increase or decrease the ORR activity of Pt−M/C catalysts, depending on which side of the volcano curve the catalyst is initially located. These fundamental insights reveal the structural origins of the combined high activity and durability achieved on solid PtNi$_3$/C catalysts.

2. EXPERIMENTAL SECTION

2.1. Catalyst Preparation. The dealloyed PtNi$_3$/C catalysts were produced via a typical synthesis route as described more fully elsewhere.[9] In brief, all the dealloyed PtNi$_3$/C catalysts were prepared via an impregnation method followed by a chemical dealloying step in acid. Several factors which were previously reported to affect the nanoporosity were varied during the preparation.[23,27,38] The factors include (1) the acid used for leaching Ni (HNO$_3$ or H$_2$SO$_4$ denoted NA or SA), (2) the atmosphere during the chemical dealloying (air or N$_2$), (3) the use of a postdealloying thermal anneal in 5% H$_2$/N$_2$ at 400 °C for 4 h, and (4) the particle size of the PtNi$_3$ precursors (Scheme 2). The aim was to not only optimize the sample preparation strategy but also produce a series of catalysts with similar core−shell structure but varied nanoporosity in an effort to perform a systematic study of the structure−activity−durability correlations of this class of catalysts.

2.2. MEA Tests. The MEAs were fabricated by a catalyst-coated diffusion media (CCDM) method.[36] The 50 cm^2 MEAs prepared above were tested for their cathode ORR kinetic activities under H$_2$/O$_2$ (anode/cathode) following the suggested protocol issued by the Department of Energy (DOE):[39] H$_2$/O$_2$ stoichiometries of 2.0 and 9.5, 100% relative humidity, cell temperature of 80 °C, and a back pressure of 150 kPa$_{abs}$. During the voltage cycling tests, 200 sccm H$_2$ (anode) and 50 sccm N$_2$ (cathode) were admitted at 150 kPa$_{abs}$. The cell voltage was swept at 50 mV s^{-1} between 0.6 and 1.0 V in a triangular profile for up to 30000 cycles (all potentials vs reversible hydrogen electrode (RHE) unless otherwise stated). The MEAs were subjected to the cathode catalytic activity (H$_2$/

## Scheme 2. Synthesis of Catalysts Studied in This Work[a]
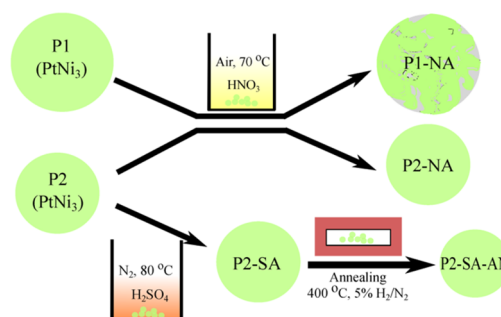
[a]The two PtNi$_3$ precursors (labeled as P1 and P2) with different particle sizes were treated in either (1) 1 M nitric acid at 70 °C for 24 h in air (P1-NA and P2-NA) or (2) 0.5 M sulfuric acid at 80 °C for 24 h in nitrogen (P2-SA). After the dealloying, some P2-SA catalysts were thermally annealed at 400 °C for 4 h in 5% H$_2$ and 95% N$_2$, labeled as P2-SA-AN.

O$_2$) and the H$_2$/air performance tests after 200 (denoted as BOL (beginning of life)), 10000 (denoted as MOL (middle of life)), and 30000 (denoted as EOL (end of life)) voltage cycles. The data collection procedures and conditions, specifically the ORR and electrochemical surface area (ECSA) measurements,[40] were performed according to the guidelines set by the USCAR Fuel Cell Tech Team (http://www.uscar.org/guest/view_team.php?teams_id=17). Specifically, the ECSAs of the cathode catalysts were obtained from hydrogen adsorption/desorption (HAD) analysis by integrating the hydrogen adsorption area over a range of 0.08−0.4 V.

2.3. Microscopy. Transmission electron microscopy in this work was performed on a JEOL 240 2100F S/TEM equipped with high-resolution polepiece (HRP) and a probe spherical aberration (Cs) corrector, giving a point resolution of 0.14 nm. High angle annular dark field (HAADF) scanning TEM (STEM) images were formed by aligning the Ronchigram with the optic axis and a 40 μm condenser aperture with the center of the Ronchigram. A camera length of 10 cm was used to minimize the effect of diffraction contrast on 247 of the HAADF images. Electron energy loss spectroscopy (EELS) analysis was performed using a postcolumn GIF Tridiem system from Gatan Inc.

2.4. Electrode Preparation and XAS Data Collection. Upon the completion of MEA testing, the MEAs were transferred to Northeastern University for XAS electrode preparation. Specifically, the cathode CCDM was detached from the membrane and then mounted into a previously described spectroelectrochemical half-cell[37] for in situ XAS measurements. Multiple layers were necessary for the Ni geometric loading to reach a ~0.05 edge height at the Ni K edge. All data were collected in the fluorescence mode with a 32-element Ge solid-state detector at beamlines X3B and X19A at the National Synchrotron Light Source (NSLS), Brookhaven National Laboratory. The 0.1 M HClO$_4$ (GFS Chemicals) electrolyte was constantly sparged with either nitrogen or oxygen gases (both high purity) while being continuously pumped through the cell. A RHE was placed in the electrolyte reservoir and connected to the cell by a salt bridge consisting of silicone tubing with a Vycor tip. The voltage cycling limits were 0.05−1.1 V vs RHE. Data collection was performed at the chosen potentials held until a steady state was reached during anodic sweeps. To refresh the surfaces after each potential hold
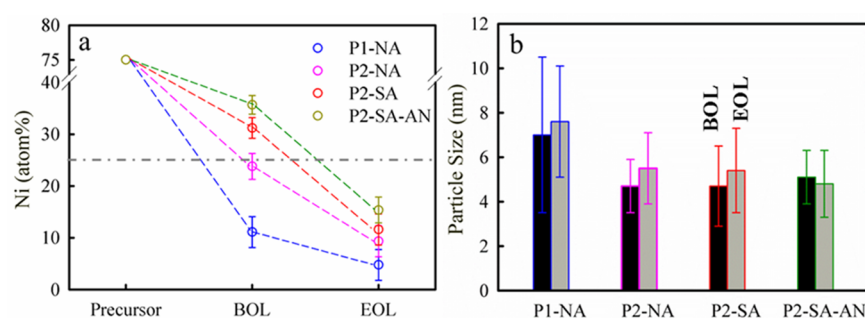
Figure 1. (a) Ni atomic percentages (Ni/(Ni + Pt) × 100%) in precursor, BOL, and 30k-cycled (denoted as EOL) MEAs, respectively, as determined by electron probe microanalysis (EPMA). The error bars represent the standard deviation of EPMA measurements among at least three different locations; the horizontal dashed line represents the saturation M content reported previously.[21] (b) Mean particle sizes of PtNi$_3$/C NPs in the MEAs at BOL and EOL stages as determined by transmission electron microscopy (TEM).[9] For each sample at least 100 particles were measured and the standard deviations are represented by the error bars. Detailed information regarding the particle size and morphology evolution during acidic pretreatment and long-term PEMFC operation is provided by our previous TEM study.[9]
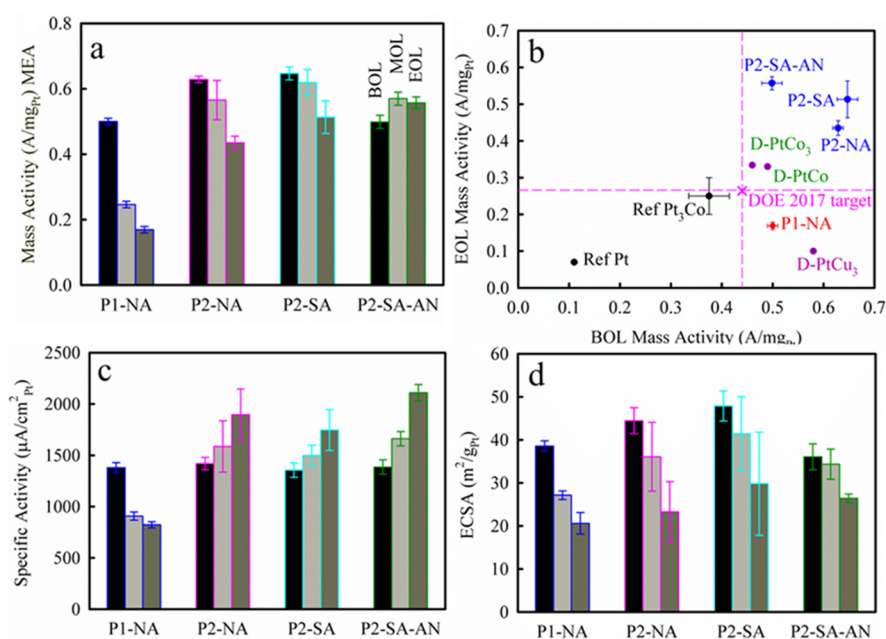
Figure 2. (a) Mass activity, (c) specific activity, and (d) electrochemical surface area (ECSA) of the four PtNi$_3$/C catalysts. The activities were measured at 0.9 V in H$_2$/O$_2$ MEAs at 80 °C, 100% relative humidity, and 150 kPa$_{abs}$ after high-frequency resistance correction; black, light gray, and dark gray represent BOL, MOL (10k-cycled), and EOL (30k-cycled) MEA, respectively. The ECSAs were obtained from hydrogen adsorption/desorption analysis by integrating hydrogen adsorption area from 0.08 to 0.40 V in cyclic voltammetry (CV). The error bars represent the standard deviations of measurements of at least four MEA samples. (b) Summary of mass activity for dealloyed catalysts from this work and from previous work on MEAs at both BOL and EOL stages: PtCu$_3$/C[45] and dealloyed PtCo$_3$/C and PtCo/C,[24] together with commercial Pt$_3$Co/C[40] and commercial Pt/C;[49] the pink cross represents the DOE 2017 targets for BOL (0.44 A mg$_{Pt}^{-1}$) and EOL mass activity (0.26 A mg$_{Pt}^{-1}$).[39]

(i.e., strip the catalytic surfaces of any accumulated oxo species), the electrode was fully cycled after each potential hold until the voltammograms were stabilized.

The alignment, background subtraction, and normalization of the XAS data were performed with the IFEFFIT suite.[41] Typical EXAFS fitting was performed using FEFF6.[42] The Δμ signals were generated using the subtractive method, Δμ = μ$_{ads}$ − μ$_{clean}$, thereby removing the absorption from the bulk of the Pt−Ni/C clusters. This relationship can be described as

$$\Delta\mu(V) = \mu(Pt, V \text{ in } N_2 \text{ or } O_2) - \mu(Pt, 0.54 \text{ V in } N_2) \tag{1}$$

where 0.54 V in N$_2$ is taken as the conditions when the Pt electrode is the cleanest or free of "ordered" adsorbates (double-layer region). The possible contribution to the XANES

scattering arising from the anions and water physisorbed on the Pt surface under these conditions is negligible owing to disorder and nonregistry with the Pt atoms on the surface.[43,44]

3. RESULTS AND DISCUSSION

The average Ni atomic percentages and particle sizes of the studied PtNi$_3$/C catalysts under different cycling stages are summarized in Figure 1. All the catalysts exhibited substantial Ni loss during the acidic pretreatment as well as the extensive voltage cycling performed in the PEMFCs, but several differences are apparent. The Ni content at both BOL and EOL stages in ascending order are P1-NA < P2-NA < P2-SA < P2-SA-AN. This Ni retention trend can be related to the different nanoporosities of these catalysts expected from the
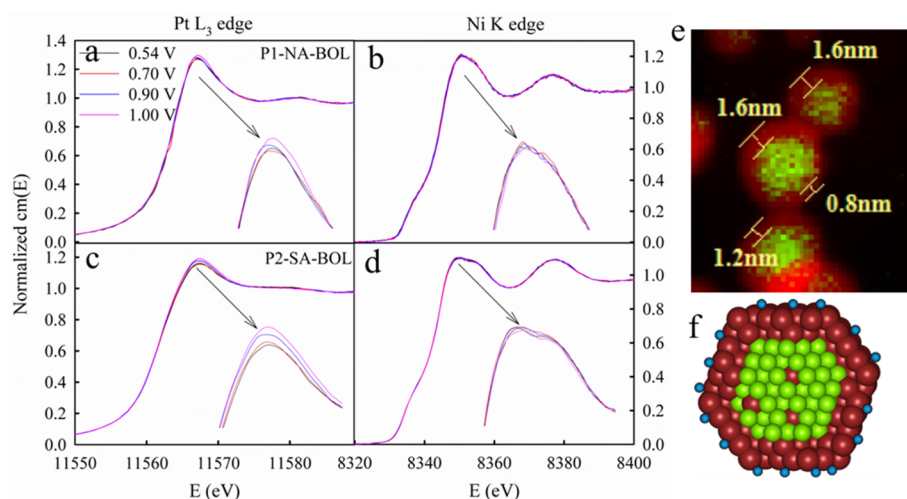
Figure 3. Pt L_3 edge (a, c) and Ni K edge (b, d) XANES spectra of P1-NA (top) and P2-SA (bottom) representing porous and solid Pt−Ni$_3$/C catalysts in O$_2$-purged 0.1 M HClO$_4$, respectively, at various potentials. (e) Examples of overlaid elemental maps of Pt (red) and Ni (green). (f) Scheme of the adsorption of oxygen on Pt surfaces at elevated potentials as revealed by in situ XANES. The blue balls represent O(H)*.

synthetic strategies. Specifically, previous HAADF STEM results[9,40] showed that the majority of the P1-derived PtNi$_3$/C NPs (P1-NA) are highly porous, whereas the P2-derived PtNi$_3$/C NPs after the same leaching process (P2-NA) are mostly solid. The significant difference in nanoporosities between these two catalysts is attributable to their different particle sizes (Figure 1b). For a given acid-leaching process and particle composition, the formation of porous percolated Pt-M NPs occurs mostly for NPs larger than the critical size (P1-NA here and previously reported PtM$_x$/C ($x > 1$) catalysts subjected to acidic pretreatment[45,46]),[23,47] whereas the NPs smaller than the critical size remain solid (P2-NA here). This is further supported by the fact that all the P2-derived PtNi$_3$/C catalysts with comparable particle sizes (Figure 1b) are dominated by solid NPs. Further, the particle sizes of the P2-derived catalysts at the EOL stage were smaller than those of the P1-NA at the BOL stage and thus also likely smaller than the critical size. Thus, the formation of nanopores is largely suppressed throughout the long-term operation.

To further reduce the nanoporosity of P2-NA, the HNO$_3$ for dealloying was replaced by H$_2$SO$_4$ (labeled as P2-SA), given that H$_2$SO$_4$ is a milder oxidant than HNO$_3$, and the switch of dealloying atmosphere (air) to nitrogen as an inert-atmosphere environment was recently demonstrated to form more solid Pt-M NPs in comparison to an oxidized environment.[23] A postannealing treatment was then performed on P2-SA (labeled as P2-SA-AN) to enhance the integrity of the Pt overlayers. As a result, the Ni contents in P2-SA and P2-SA-AN at the BOL stage are well above the saturation value reported on previous dealloyed Pt$_x$M/C ($x > 1$) catalysts,[21] and those at the EOL stage are still higher than that of P1-NA at the BOL stage, indicating a drastic increase in Ni retention. The expected nanoporosity trend within these catalysts, P1-NA > P2-NA > P2-SA > P2-SA-AN, was also confirmed by the increasing potential required for the oxygen species to penetrate into the Pt shells and interact with Ni in the core[48] and is consistently related to the Ni retention trend: P1-NA < P2-NA < P2-SA < P2-SA-AN. This correlation was also found on the PtCo$_3$/C catalysts subjected to analogous synthetic processes.[40] These results suggest that the M retention of Pt−M systems with given compositions during the acidic pretreatment and MEA

operation are governed by the nanoporosity of the NPs and thereby can be manipulated by tuning the synthesis and dealloying parameters.

The electrochemical performances of the studied catalysts obtained in PEMFCs following the aforementioned DOE protocol[39] are summarized in Figure 2. Figure 2a shows that the mass activity of P1-NA at the EOL stage is below the DOE 2017 targets[39] owing to the drastic activity loss (~66%) upon long-term operation, whereas the mass activities of all the P2-derived PtNi$_3$/C catalysts at both BOL and EOL stages far exceed the DOE targets.[39] The exceptional performance of P2-derived catalysts in PEMFCs is further highlighted in Figure 2b, summarizing the performance of previously reported dealloyed PtM$_x$/C,[24,45] commercial Pt/C,[49] and Pt$_3$Co/C[40] catalysts. It is noteworthy that the initially high ORR mass activity (0.50 A mg$_{Pt}^{-1}$) of P2-SA-AN further increases to 0.56 A mg$_{Pt}^{-1}$ after 30k cycles in a PEMFC. This differs from all the previously reported Pt-based catalysts, whose mass activities decrease after long-term operation in MEAs.[12,13,45] Thus, the severe activity degradation of dealloyed PtM$_x$/C catalysts induced by M dissolution upon long-term operation in MEAs is curtailed, despite the substantial Ni dissolution (Figure 1a). It is thus of particular interest to understand the unique mass activity trend exhibited by P2-SA-AN.

The poor durability of the porous P1-NA arises from the drastic drop in the specific activity and ECSA during MEA operation (Figure 2c,d), which can be attributed to the attenuation of strain and/or ligand effects caused by the loss of M (Figure 1a) as well as particle growth (Figure 1b) and/or smoothing, respectively, according to previous studies on various Pt−M/C systems.[13,21,32,45] This widely accepted degradation mechanism apparently is not applicable to the solid P2-derived PtNi$_3$/C catalysts, for which the specific activity increases upon cycling (Figure 2c) in spite of the Ni loss (Figure 1a). The increasing specific activity trend, in addition to the moderate ECSA loss (Figure 2d), expresses the exceptional durability of the P2-derived catalysts.

Although much information on the particle morphology evolution of P2-derived catalysts during cycling has been provided via ex situ microscopy methods,[9,40] the structural origin of the increasing specific activity trend is unclear. This is

mainly because the specific activities of Pt−M systems are usually coimpacted by strain, ligand, and particle size effects,[24] which significantly complicate the activity−property correlations. In situ XAS has been employed here to elucidate these properties, as it provides comprehensive insights into the interplay of the three effects in Pt−M/C systems under reactive conditions.[21,24]

The structural evolution of the four PtNi₃/C catalysts upon extensive cycling in a MEA as per DOE protocol was studied by conducting systematic in situ XAS studies at three different cycling stages (post-MEA: BOL (200 cycles), MOL (10k cycles), and EOL (30k cycles)). For all of the catalysts, the Pt white line intensity increases at higher potentials (Figure 3a) owing to the charge transfer from exposed Pt to the oxygenated species (such as s O(H)*) accumulated on the surface at elevated potentials.[10,50,51] In contrast, the changes at the Ni K edge with potentials (Figure 3b) are minimal. This indicates that the majority of Ni atoms are located inside the NPs without being directly exposed to the electrochemical environment, as expected from the selective Ni dissolution during the acidic pretreatment. These results confirm that the core−shell structure (Pt$_{surf}$@PtNi$_{core}$) of the catalysts reported from the HAADF STEM analysis (Figure 3e) is maintained during the in situ XAS data collection. The HAADF STEM analysis did not present evidence of the formation of hollow NPs, which were shown to exhibit enhanced ORR activity and durability in comparison to Pt/C.[52−55] The HAADF STEM study also indicated that the Pt overlayer thicknesses of all the catalysts is greater than ∼1 nm (approximately 4−5 atomic layers). Ligand effects can thereby be excluded owing to their short effective ranges.[28] On the other hand, strain effects over much longer effective ranges are widely believed to play a dominant role for ORR activity enhancement of Pt−M/C systems with core−shell structures.[11,20,21]

The evolution of the local environments including the first-shell bond distance and coordination number in the PtNi₃/C catalysts as a function of long-term PEMFC operation has been quantitatively evaluated via in situ EXAFS analysis. The veracity of these analyses is justified by the good fit quality shown by Figure 4 in conjunction with the physically meaningful fitting values summarized in Table S1 in the Supporting Information. The P1-NA and P2-SA-AN catalysts at the BOL and EOL stages (representing porous and solid NPs, respectively) are presented in Figure 4 for comparative purposes. A fully detailed accounting of the EXAFS fitting parameters, including the best-fit values for all of the catalysts, is provided in the Supporting Information.

The bulk average Pt−Pt bond distances (R_{PtPt}(s)) obtained from EXAFS analysis have been demonstrated as a valid descriptor for strain effects for Pt−M/C systems.[21] The R_{PtPt}(s) values summarized in Figure 5a are linearly related to the Ni content of the catalysts as governed by Vegard's law (Figure 5b).[56] Since the strain represented by the shortened R_{PtPt} (Figure 5a) is governed by the content of Ni that is alloyed with Pt, the strain attenuation with cycling represented by R_{PtPt} relaxation (Figure 5a) accordingly arises from Ni dissolution. The Ni dissolution also drastically changes the local coordinate environment of Pt (Figure 5c,d). The decrease of the first-shell Pt−Ni coordination number (N_{PtNi}) with Ni dissolution (Figure 5d) is expected, as N_{PtNi} is codetermined by the Pt/Ni atomic ratio and atomic distribution.[57] The concomitant increase of N_{PtPt} in P2-derived catalysts (Figure 5c) suggests that the surface diffusion of Pt is sufficiently fast in comparison
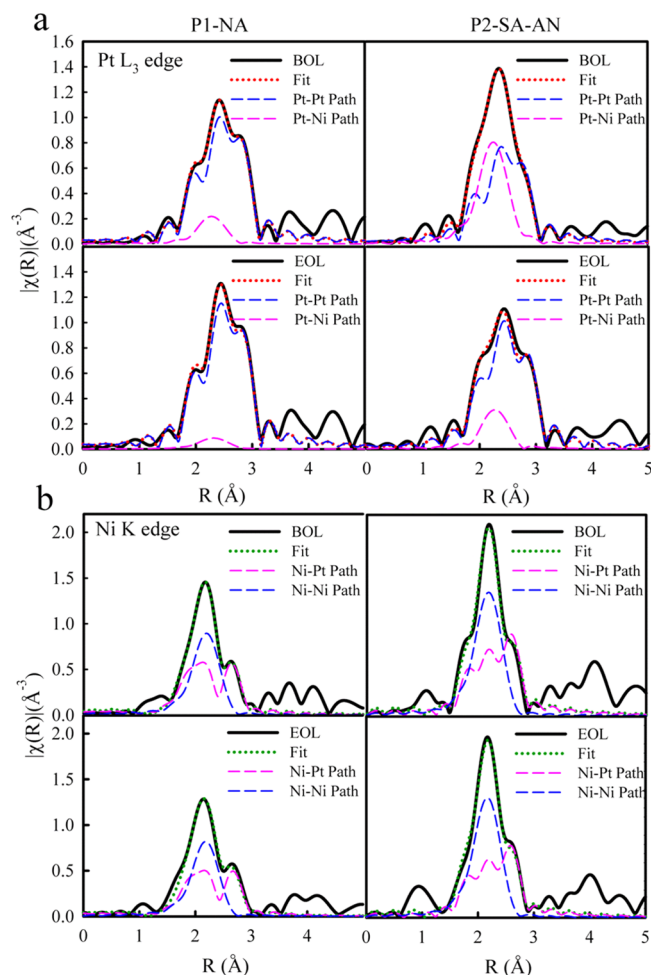

Figure 4. Pt L₃ edge (a) and Ni K edge (b) FT-EXAFS spectra collected in 0.1 M HClO₄ electrolyte at 0.54 V and the corresponding least-squares fits for P1-NA (left column) and P2-SA-AN (right column) catalysts representing porous and solid NPs, respectively, under different voltage cycling stages: BOL (top) and EOL (bottom).

to the leaching rate of Ni (despite the initially high Ni content), and consequently the pores resulting from Ni leaching are filled with Pt atoms.[47] This is consistent with previous HAADF STEM results that the P2-derived PtNi₃/C NPs maintain low nanoporosity over the course of the 30k voltage cycles in MEAs.[9]

Unlike R_{PtPt}, both N_{NiNi}(s) and R_{NiNi}(s) that exist exclusively in the core remain largely unchanged during cycling despite the reduction in Ni content (Figure 6), and the R_{NiNi}(s) values are close to those calculated using the Ni content in the PtNi₃ precursor (75%) based on Vegard's law (Figure 6a). These results clearly show that the lattice constant of the core in Pt-M/C systems is governed by the precursor composition and is not altered by M dissolution. This is strikingly different from the Pt shells, whose lattice constant increases with M dissolution (Figure 5a). These results together provide unequivocal evidence for the lattice mismatch between the M-rich core and Pt-rich shells in Pt−M/C systems, as well as the strain induced by the lattice mismatch.

As the R_{PtPt} value increases following voltage cycling as a consequence of Ni dissolution, the specific activity of P1-NA drops rapidly, whereas the specific activities of P2-derived catalysts gradually increase (Figure 2c). Together these two
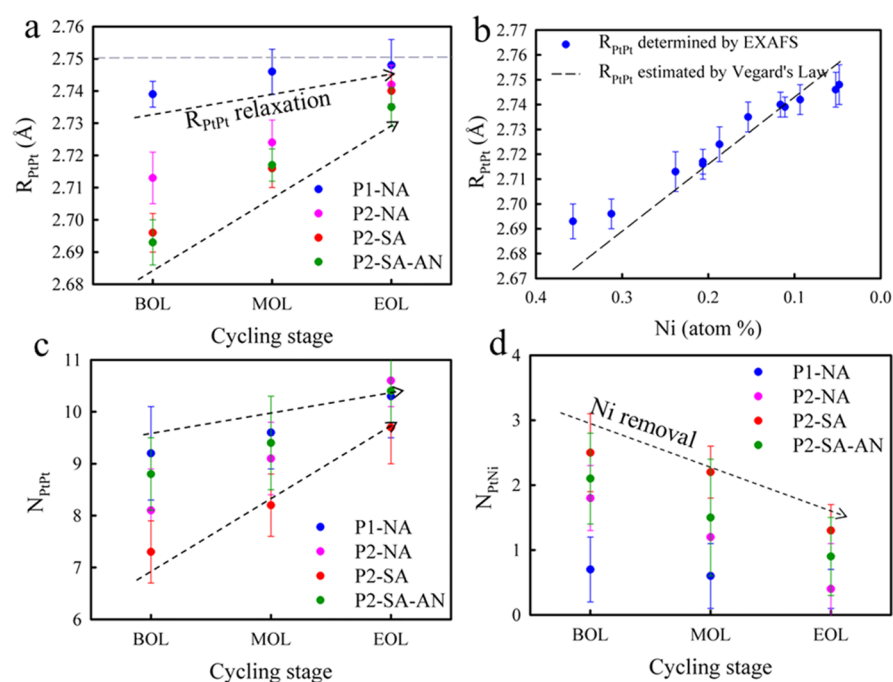
Figure 5. (a) Bulk average Pt−Pt bond distance (R_{PtPt}) obtained by EXAFS fitting (R_{PtPt}) of studied PtNi$_3$/C catalysts at BOL, MOL, and EOL stages. The horizontal dashed line represents the R_{PtPt} value (2.75 Å) of small Pt/C NPs (∼3 nm).[10] The different R_{PtPt} relaxation rates upon cycling of P1- and P2-derived catalysts are highlighted by the dashed arrow lines. (b) Experimental R_{PtPt}(s) (blue dots) presented in comparison to those calculated using the Ni atomic content obtained by EPMA based on Vegard's law (black dashed line). Coordination numbers of (c) Pt−Pt and (d) Pt−Ni obtained by EXAFS fitting at BOL, MOL, and EOL stages. The vertical error bars are produced by the EXAFS fitting.
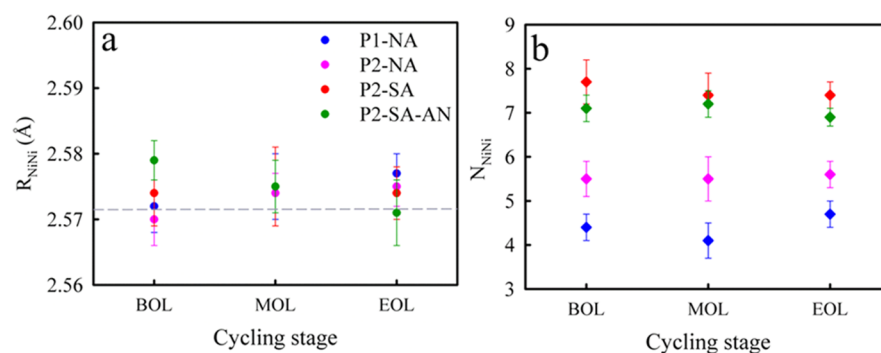
Figure 6. First-shell Ni−Ni bond distance (a) and coordination number (b) obtained by EXAFS fitting of studied PtNi$_3$/C catalysts at BOL, MOL, and EOL stages. The horizontal dashed line in (a) represents the R_{NiNi} value (2.572 Å) calculated using the Ni relative content in the precursor (0.75) on the basis of Vegard's law. The vertical error bars are produced by the EXAFS fitting.

trends form a volcano curve of specific activity as a function of R_{PtPt} (Figure 7). This volcano curve resembles the volcano-type activity plots (Scheme 1) that have been reported on a wide variety of materials, including Pt alloys.[58] The porous P1-NA initially has low Ni content and long R_{PtPt} at the BOL stage due to the substantial loss of Ni during the acidic pretreatment. Its specific activity is located on the Pt−O strong binding leg of the volcano owing to the weak strain effects and downshifts toward that of the pure Pt/C with cycling due to further Ni dissolution (or strain attenuation). Only a trivial amount of Ni remains in P1-NA after 30k cycles at the EOL stage, leaving behind essentially a Pt-like structure with R_{PtPt} values close to that of pure Pt/C NPs (∼2.75 Å).[22] Consequently, the SA (822 μA/cm$_{Pt}^2$) and ECSA (21 m^2/g$_{Pt}$) values of the 30k-cycled porous P1-NA are essentially the same as those (SA, 787 μA/cm$_{Pt}^2$; ECSA, 23 m^2/g$_{Pt}$) of the 30k-cycled 30 wt % Pt/C,[49] indicating a complete loss of the specific activity enhancement. This

decreasing specific activity trend with M loss (or strain relaxation) was also reported on dealloyed PtCo$_x$/C[21] and PtCu$_x$/C[20] catalysts, depicting the descending portion of a volcano curve. On the other hand, the solid P2-derived PtNi$_3$/C catalysts not only begin with a comparably higher Ni concentration and shorter R_{PtPt}(s) at the BOL stage but also retain far more Ni after 30k cycles, strikingly different from the case for porous PtM$_x$/C catalysts. Thus, the increasing specific activity trend of P2-derived catalysts with cycling is explained as the specific activity moves toward the apex along with the ascending Pt−O weak binding leg of the volcano (Scheme 1) with Ni dissolution or strain attenuation. The P2-derived catalysts located on the Pt−O weak binding leg of the Sabatier volcano curve proposed here agree with previous studies showing that Pt$_3$M (M = Fe, Co, Ni, etc.) catalysts are located on the Pt−O weak binding leg,[17,59] given that the Ni contents
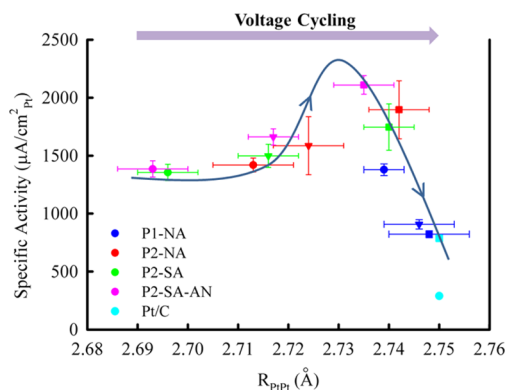
Figure 7. Specific ORR activity trend as a function of R_{PtPt} of studied $PtNi_3/C$ catalysts and reference Pt/C MEAs.[49] The data collected at the BOL, MOL, and EOL stages are represented by dots, triangles, and squares, respectively. It is noted that the solid arrow curve is a guide to the eye and by no means implicates the precise location of the apex. The horizontal error bars are produced by the EXAFS fitting, and the vertical error bars represent the standard deviations of multiple measurements of specific activities.

of P2-derived catalysts at the BOL stage are around (P2-NA) or above 25% (P2-SA and P2-SA-AN) (Figure 1a).

The particle size effects also make some contributions to the increase of the specific activity of P2-derived catalysts with cycling, given that all the catalysts underwent particle growth (Figure 1b) and/or surface smoothing (removal of under-coordinated atoms via electrochemical "annealing") during cycling, as evidenced by the ECSA reduction (Figure 2d). Indeed, the specific activity of small Pt/C NPs (~2 nm) increases up to 4-fold upon extensive cycling, but the activity gain is compensated for by a drastic loss of ECSA up to ~75%.[49] However, the particle size effects largely diminish for Pt/C NPs larger than 3 nm, and accordingly the specific activity slowly increases in a linear manner as the particle grows from ~3 nm until reaching saturation at ~11 nm.[60−62] We thus postulate that particle size effects are minimal in affecting the specific activity of the studied catalysts dominated by large NPs (≥5 nm; Figure 1b) in comparison to the concurrent strain effects. This hypothesis is supported by the rapid drop of the specific activity of P1-NA with cycling (Figure 2c), which reflects that the specific activity gain from particle size effects is overwhelmed by the loss caused by strain attenuation. As for the P2-derived $PtNi_3/C$ catalysts, they exhibit even lower ECSA reductions (weaker particle size effects) but higher R_{PtPt} relaxations (stronger strain attenuation) with cycling in comparison to P1-NA (Figure 8). Therefore, the particle size effects in the P2-derived $PtNi_3/C$ catalysts shall also be overwhelmed by the strain effects and do not play a major role in the increase of the specific activity following extensive voltage cycling.

The Sabatier volcano-type behavior of the specific activities of the $PtNi_3/C$ catalysts has been further studied by the surface-sensitive $\Delta\mu$ analysis, which identifies the key ORR intermediates on the Pt surface and simultaneously estimates the relative coverage(s) of the intermediates represented by $\Delta\mu$ amplitude ($|\Delta\mu|$) as a function of applied potential.[22,50,63] The $|\Delta\mu|$ value obtained at 0.9 V in the N_2-saturated electrolyte (denoted as $|\Delta\mu|_N$; Figure 9a) represents the coverage of oxygenated adsorbates arising exclusively from water activation (denoted as Θ_{O*}):
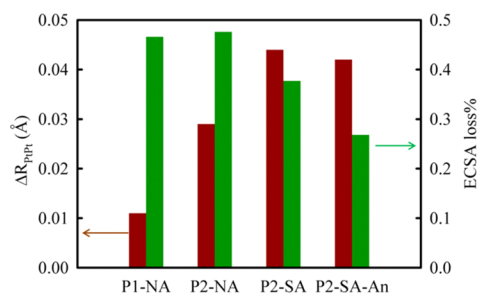
Figure 8. Increase in R_{PtPt} (e.g. $\Delta R_{PtPt} = R_{PtPt}^{EOL} - R_{PtPt}^{BOL}$) (brown) as well as the relative loss of ECSA (e.g., $(ECSA_{BOL} - ECSA_{EOL})/ECSA_{BOL} \times 100\%$) (green) for the studied catalysts subjected to 30k cycles in PEMFCs.

$$H_2O_{ads} \rightarrow OH_{ads} + H^+ + e^- \qquad (2)$$
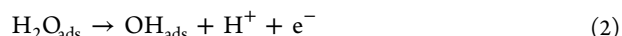
and tracks with the Pt−O binding energy.[50,64] This reaction is driven by the potential difference between the associated $Pt(H_2O)/Pt-OH_{ads}$ redox potential E_{redox} and the applied potential E.[33] The available active sites as a function of E can be expressed as[33]

$$N_{active} = N_{total} \frac{1}{1 + e^{F/RT(E-E_{redox})}} \qquad (3)$$

where N_{active} and N_{total} are the available and total numberd of surface active sites, respectively, F is the Faraday constant, R is the universal gas constant, and T is the temperature. Therefore, the fraction of the active sites occupied by OH_{ads} at the applied potential E is

$$\Theta_{O*} = \frac{N_{total} - N_{active}}{N_{total}} = \frac{1}{1 + e^{-F/RT(E-E_{redox})}} \qquad (4)$$

This equation ignores the repulsive effect between the adjacent adsorbed species on a Pt surface,[65] which becomes significant at high potentials and therefore makes the dependence of Θ_{O*} on E more spread out. As noticed immediately, the experimental $|\Delta\mu|_N$ value as a function of R_{PtPt} (Figure 9a) generally follows the calculated trend of Θ_{O*} at 0.9 V as a function of the E_{redox} value derived from eq 4 (Figure 9b). More specifically, the rapid increase of the $|\Delta\mu|_N$ value of P1-NA with cycling resembles the steep Θ_{O*} curve where the E_{redox} value is comparable to 0.9 V (Figure 9b), whereas the $|\Delta\mu|_N$ value of P2-derived catalysts is largely suppressed in comparison to that of P1-NA and does not change drastically with R_{PtPt}, which matches the gradual Θ_{O*} curve where the E_{redox} value is notably higher than 0.9 V (Figure 9b). This can be well understood, as the strain represented by R_{PtPt} weakens the Pt−O binding energy, thereby positively shifting the redox potential E_{redox}. Indeed, it was previously shown that the E_{redox} value (or the applied potential at which the Θ_N value is equal to 0.5 according to eq 4) for Pt in acid electrolyte is positively shifted from ~0.85 to ~0.95 V by alloying with Ni, resulting in a drastic reduction in Θ_{O*}.[7,33] Interestingly, the $|\Delta\mu|$ value obtained at 0.9 V in O_2-saturaed electrolyte ($|\Delta\mu|_O$) is higher than $|\Delta\mu|_N$ for P2-derived catalysts but comparable to that for P1-NA. As both O_2 dissociation and water activation may contribute to $|\Delta\mu|_O$, the difference between $|\Delta\mu|_O$ and $|\Delta\mu|_N$ is attributed to the adsorption of molecular oxygenated species $((H)OOH*)$.[66] This suggests that the Pt−O binding energy is overly weakened by the high surface strain and the rate-determining step involves breaking the O_2 bond. On the other hand, the trivial difference between $|\Delta\mu|_O$ and $|\Delta\mu|_N$ for P1-NA
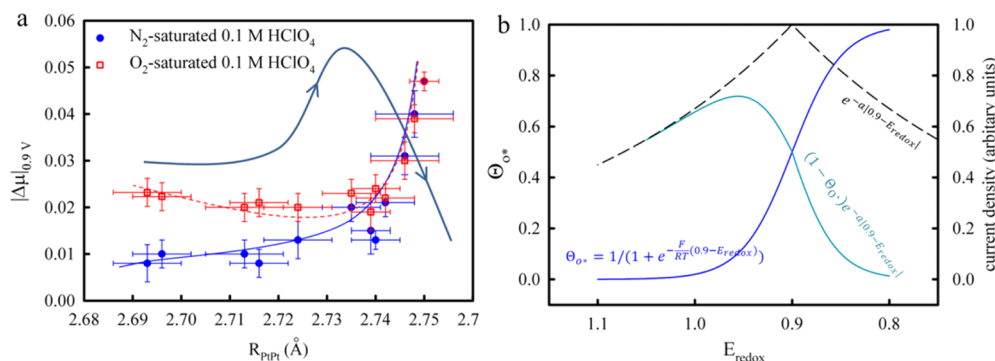
Figure 9. (a) Plot of $|\Delta\mu|$ obtained from the peak heights around 0−5 eV above the Pt L$_3$ edge for the studied PtNi$_3$/C catalysts at BOL, MOL, and EOL stages at 0.9 V in N$_2$-saturated (blue solid dots) or O$_2$-saturated (red open squares) in the 0.1 M HClO$_4$ electrolyte. The lines are drawn as guides to the eye. The horizontal and vertical error bars are produced by the EXAFS fitting and multiple $\Delta\mu$ XANES measurements. The solid arrow curve derived from Figure 7 depicting the specific activity trend of studied catalysts as a function of R_{PtPt} is presented here to manifest the correlation between the activity and the coverage of adsorbed oxygen species represented by $|\Delta\mu|$. Catalysts are not differentiated here; plots with catalysts differentiated by colors are given in Figure S9 in the Supporting Information. (b) Plot of Θ_{O*} derived from eq 4 assuming the optimal redox potential of 0.9 V and a temperature of 298 K: the reaction kinetic factor $\exp(-a|V - E_{redox}|)$ with a set to be 4 to give a reasonable volcano shape and the combined site-blocking effect and kinetic effect $(1 - \Theta_{O*}) \exp(-a|V - E_{redox}|)$.

indicates that the Pt surface is predominately covered by OH$_{ads}$ from water activation and the desorption of OH$_{ads}$ limits the ORR rate. It is worth noting that the coverage of the molecular oxygen species, represented by $|\Delta\mu|_O - |\Delta\mu|_N$, is low for all of the studied catalysts. This is attributable to the slower decline in the O$_2$ dissociation rate with Pt−O bond weakening relative to the drop-off rate of O(H)* adsorption.[67] As a result, the Θ_{O*} value exhibits an asymmetric behavior as a function of Pt−O binding energy, which essentially determines the asymmetric Sabatier volcano-type behavior of the specific activity of the studied dealloyed PtNi$_3$/C catalysts (Figure 9a) as shown below.

For a surface redox mediated electrocatalytic process (ORR here) with potential-dependent population of active sites, the general rate expression that considers the site-blocking effect will have the form[33]

$$J \propto N_{total}(1 - \Theta_{O*}) \exp\left(-\frac{\Delta H^*}{RT}\right) \exp\left(-\frac{E - E^\circ}{b}\right) \quad (5)$$

where J is the cathode current density, Θ_{O*} is the coverage by adsorbed oxygen species at potential E, ΔH^* is the activation entropy for the slow step in the electrocatalytic process, E° is the standard potential for the Faradaic process, and b is the value of the Tafel slope. The site-blocking effect lies in the pre-exponential factor $(1 - \Theta_{O*})$. The kinetic effect lies in the exponential factor in the second term, $\exp(-\Delta H^*/RT)$, which can be rewritten as $\exp(-a|V - E_{redox}|)$, where a is a constant parameter determining the volcano shape and V is the optimized redox potential corresponding to the minimized ΔH^*. This exponential factor gives a symmetric volcano curve as a function of E_{redox} centered at V (Figure 9b). The V value is chosen to be the targeted potential 0.9 V here, given that it is suggested to be in the range of 300−400 mV lower than the E° value of the ORR (1.23 V).[33] More importantly, the inclusion of the site-blocking effect, i.e. the pre-exponential factor $(1 - \Theta_{O*})$ where Θ_{O*} is derived from eq 4, leads to an asymmetric volcano curve that resembles the skewed volcano curve observed experimentally (Figure 9a). Although a rather simplified conceptual model is used here, it adequately demonstrates that the skewed Sabatier volcano curve toward the Pt−O weak leg is essentially induced by the asymmetric

nature of Θ_{O*}. As the rapid decrease of the specific activity of P1-NA with cycling closely tracks $1 - |\Delta\mu|_O$, it indicates that the site-blocking effect is the dominant effect that limits the ORR. On the other side of the volcano, the specific activity of P2-derived catalysts decrease with much slower rates when moving away from the apex because the site-blocking effect is now largely suppressed owing to the low Θ_{O*} coverage.

The demonstration of the asymmetric Sabatier volcano-type behavior on practical catalysts under PEMFC operating conditions provides new insights into the subtle interplay between the activity and durability of Pt−M/C catalysts. This indicates that if the Pt−O bond strength is insufficiently weakened by inadequate M content in Pt−M/C systems (such as with the P1-derived PtNi$_3$/C catalysts), the specific activity will drop drastically along the steep Pt−O strong binding leg with M dissolution. On the other hand, even if the Pt−O bond strength is overly weakened by the excessive M in Pt−M systems (such as with the P2-derived PtNi$_3$/C catalysts), the specific activity will not be far inferior to the apex value, as determined by the gradual nature of the Pt−O weak leg, whereas the durability will be significantly improved as the M dissolution with cycling results in an activity increase until reaching the apex. This is the fundamental determinant of the combined high activity and durability demonstrated on the solid PtNi$_3$/C catalysts. As mentioned above, the activities of the PtNi$_3$/C and PtCo$_3$/C catalysts after the same synthetic methods are essentially the same.[40] This is expected, as the Ni or Co alters the ORR rate indirectly by changing the electronic properties of Pt surfaces via strain effects rather than directly participating in the ORR. Therefore, the fundamental structure−activity−durability correlation observed on PtNi$_3$/C catalysts can be extended to other Pt-alloy systems with core−shell structures. More generally, the asymmetric volcano curve of catalysis revealed here may be extended to any surface redox mediated electrocatalytic process with potential-dependent population of active sites such as the ORR promoted by transition-metal chelates,[68] thereby providing a fundamental basis for the rational design of a wide variety of catalytic materials.

4. CONCLUSIONS

We have shown that the degradation of Pt−M/C catalysts during long-term PEMFC operation can be largely mitigated with only minimal compromises in activity by manipulating the nanoporosity of Pt-M/C catalysts. As revealed by the application of our unique post-mortem analysis, the fundamental basis of the inherent high activity and durability of the solid $PtNi_3$/C catalysts lies in the skewed volcano nature of Sabatier's principle of catalysis owing to the site-blocking effect. Long-term operation in PEMFCs shifts the dealloyed Pt−M/C catalysts toward the stronger Pt−O bond direction through removal of subsurface M, either away from or toward the apex of the Sabatier volcano depending on the initial and final M content. As for Pt−M/C NPs with excessive M confined in the cores, the specific activity climbs up gradually along the Pt−O weak side toward the apex of the volcano during PEMFC operation, whereas the specific activities of the Pt−M/C NPs with inadequate M concentrations drastically shift downward along the sharp Pt−O strong leg away from the apex. The extraordinary durability of the solid $PtNi_3$/C catalysts is therefore primarily attributed to their integrated Pt overlayers that well protect the Ni in the cores against acidic pretreatment and long-term operation, leading to higher Ni content at both the BOL and EOL stages. The new insights into these fundamental structure−activity−durability relationships will hopefully contribute to the timely development of economically viable Pt-based catalysts for PEMFC applications.

■ ASSOCIATED CONTENT

Ⓢ Supporting Information

The Supporting Information is available free of charge on the ACS Publications website at DOI: 10.1021/acscatal.5b02750.

> Additional information including the raw XAS spectra at the Pt L_3 and Ni K edges and the EXAFS fitting parameters and results (PDF)

■ AUTHOR INFORMATION

Corresponding Author

*S.M.: e-mail, s.mukerjee@neu.edu; tel, (617)373-2382.

Notes

The authors declare no competing financial interest.

■ ACKNOWLEDGMENTS

■ REFERENCES

(1) Debe, M. K. *Nature* **2012**, *486*, 43−51.

(2) Gasteiger, H. A.; Marković, N. M. *Science* **2009**, *324*, 48−49.

(3) Wagner, F. T.; Lakshmanan, B.; Mathias, M. F. *J. Phys. Chem. Lett.* **2010**, *1*, 2204−2219.

(4) Gasteiger, H. A.; Kocha, S. S.; Sompalli, B.; Wagner, F. T. *Appl. Catal., B* **2005**, *56*, 9−35.

(5) Mukerjee, S.; Srinivasan, S. *J. Electroanal. Chem.* **1993**, *357*, 201−224.

(6) Koh, S.; Strasser, P. *J. Am. Chem. Soc.* **2007**, *129*, 12624−12625.

(7) Stamenkovic, V. R.; Fowler, B.; Mun, B. S.; Wang, G.; Ross, P. N.; Lucas, C. A.; Marković, N. M. *Science* **2007**, *315*, 493−497.

(8) Stamenkovic, V. R.; Mun, B. S.; Arenz, M.; Mayrhofer, K. J. J.; Lucas, C. A.; Wang, G.; Ross, P. N.; Markovic, N. M. *Nat. Mater.* **2007**, *6*, 241−247.

(9) Han, B.; Carlton, C. E.; Kongkanand, A.; Kukreja, R. S.; Theobald, B. R.; Gan, L.; O'Malley, R.; Strasser, P.; Wagner, F. T.; Shao-Horn, Y. *Energy Environ. Sci.* **2015**, *8*, 258−266.

(10) Mukerjee, S.; Srinivasan, S.; Soriaga, M. P.; McBreen, J. *J. Phys. Chem.* **1995**, *99*, 4577−4589.

(11) Oezaslan, M.; Hasché, F.; Strasser, P. *J. Phys. Chem. Lett.* **2013**, *4*, 3273−3291.

(12) Hasché, F.; Oezaslan, M.; Strasser, P. *J. Electrochem. Soc.* **2012**, *159*, B25−B33.

(13) Mani, P.; Srivastava, R.; Strasser, P. *J. Power Sources* **2011**, *196*, 666−673.

(14) Oezaslan, M.; Strasser, P. *J. Power Sources* **2011**, *196*, 5240−5249.

(15) Sasaki, K.; Naohara, H.; Choi, Y.; Cai, Y.; Chen, W.-F.; Liu, P.; Adzic, R. R. *Nat. Commun.* **2012**, *3*, 1115.

(16) Zhang, J.; Sasaki, K.; Sutter, E.; Adzic, R. R. *Science* **2007**, *315*, 220−222.

(17) Greeley, J.; Stephens, I. E. L.; Bondarenko, A. S.; Johansson, T. P.; Hansen, H. A.; Jaramillo, T. F.; Rossmeisl, J.; Chorkendorff, I.; Nørskov, J. K. *Nat. Chem.* **2009**, *1*, 552−556.

(18) Hernandez-Fernandez, P.; Masini, F.; McCarthy, D. N.; Strebel, C. E.; Friebel, D.; Deiana, D.; Malacrida, P.; Nierhoff, A.; Bodin, A.; Wise, A. M.; Nielsen, J. H.; Hansen, T. W.; Nilsson, A.; StephensIfan, E. L.; Chorkendorff, I. *Nat. Chem.* **2014**, *6*, 732−738.

(19) Escudero-Escribano, M.; Verdaguer-Casadevall, A.; Malacrida, P.; Grønbjerg, U.; Knudsen, B. P.; Jepsen, A. K.; Rossmeisl, J.; Stephens, I. E. L.; Chorkendorff, I. *J. Am. Chem. Soc.* **2012**, *134*, 16476−16479.

(20) Strasser, P.; Koh, S.; Anniyev, T.; Greeley, J.; More, K.; Yu, C.; Liu, Z.; Kaya, S.; Nordlund, D.; Ogasawara, H.; Toney, M. F.; Nilsson, A. *Nat. Chem.* **2010**, *2*, 454−460.

(21) Jia, Q.; Liang, W.; Bates, M. K.; Mani, P.; Lee, W.; Mukerjee, S. *ACS Nano* **2015**, *9*, 387−400.

(22) Jia, Q.; Ramaker, D. E.; Ziegelbauer, J. M.; Ramaswamy, N.; Halder, A.; Mukerjee, S. *J. Phys. Chem. C* **2013**, *117*, 4585−4596.

(23) Gan, L.; Heggen, M.; O'Malley, R.; Theobald, B.; Strasser, P. *Nano Lett.* **2013**, *13*, 1131−1138.

(24) Jia, Q.; Caldwell, K.; Strickland, K.; Ziegelbauer, J. M.; Liu, Z.; Yu, Z.; Ramaker, D. E.; Mukerjee, S. *ACS Catal.* **2015**, *5*, 176−186.

(25) Dubau, L.; Maillard, F.; Chatenet, M.; Guetaz, L.; André, J.; Rossinot, E. *J. Electrochem. Soc.* **2010**, *157*, B1887−B1895.

(26) Dubau, L.; Maillard, F.; Chatenet, M.; André, J.; Rossinot, E. *Electrochim. Acta* **2010**, *56*, 776−783.

(27) Cui, C.; Gan, L.; Neumann, M.; Heggen, M.; Roldan Cuenya, B.; Strasser, P. *J. Am. Chem. Soc.* **2014**, *136*, 4813−4816.

(28) Kitchin, J. R.; Nørskov, J. K.; Barteau, M. A.; Chen, J. G. *Phys. Rev. Lett.* **2004**, *93*, 156801.

(29) Schlapka, A.; Lischka, M.; Groß, A.; Käsberger, U.; Jakob, P. *Phys. Rev. Lett.* **2003**, *91*, 016101.

(30) Hammer, B.; Nørskov, J. K.; Bruce, C.; Gates, H. K. *Adv. Catal.* **2000**, *45*, 71−129.

(31) Jia, Q.; Caldwell, K.; Ziegelbauer, J. M.; Kongkanand, A.; Wagner, F. T.; Mukerjee, S.; Ramaker, D. E. *J. Electrochem. Soc.* **2014**, *161*, F1323−F1329.

(32) Chen, S.; Gasteiger, H. A.; Hayakawa, K.; Tada, T.; Shao-Horn, Y. *J. Electrochem. Soc.* **2010**, *157*, A82−A97.

(33) Gottesfeld, S. *ECS Trans.* **2014**, *61*, 1−13.

(34) Yano, H.; Song, J. M.; Uchida, H.; Watanabe, M. *J. Phys. Chem. C* **2008**, *112*, 8372−8380.

(35) Sabatier, P. *Ber. Dtsch. Chem. Ges.* **1911**, *44*, 1984−2001.

(36) Yan, S. G.; Doyle, J. C. US Patent 0163920 A1, 2005.

(37) Arruda, T. M.; Shyam, B.; Lawton, J. S.; Ramaswamy, N.; Budil, D. E.; Ramaker, D. E.; Mukerjee, S. *J. Phys. Chem. C* **2010**, *114*, 1028−1040.

(38) Oezaslan, M.; Heggen, M.; Strasser, P. *J. Am. Chem. Soc.* **2012**, *134*, 514−524.

(39) DOE *Hydrogen and Fuel Cell Activities, Progress, and Plans*; United States Department of Energy: Washington, DC, 2009.

(40) Kongkanand, A.; Wagner, F. 2014 Annual Merit Review, US Department of Energy Hydrogen and Fuel Cells Program (accessed July 30, 2014); http://www.hydrogen.energy.gov/pdfs/review14/fc087_kongkanand_2014_o.pdf.

(41) Newville, M. *J. Synchrotron Radiat.* **2001**, *8*, 322−324.

(42) Ankudinov, A. L.; Ravel, B.; Rehr, J. J.; Conradson, S. D. *Phys. Rev. B: Condens. Matter Mater. Phys.* **1998**, *58*, 7565−7576.

(43) Wiltshire, R. J. K.; King, C. R.; Rose, A.; Wells, P. P.; Hogarth, M. P.; Thompsett, D.; Russell, A. E. *Electrochim. Acta* **2005**, *50*, 5208−5217.

(44) Roth, C.; Martz, N.; Buhrmester, T.; Scherer, J.; Fuess, H. *Phys. Chem. Chem. Phys.* **2002**, *4*, 3555−3557.

(45) Yu, Z.; Zhang, J.; Liu, Z.; Ziegelbauer, J. M.; Xin, H.; Dutta, I.; Muller, D. A.; Wagner, F. T. *J. Phys. Chem. C* **2012**, *116*, 19877−19885.

(46) Jia, Q.; Caldwell, K.; Ramaker, D. E.; Ziegelbauer, J. M.; Liu, Z.; Yu, Z.; Trahan, M.; Mukerjee, S. *J. Phys. Chem. C* **2014**, *118*, 20496−20503.

(47) Erlebacher, J.; Aziz, M. J.; Karma, A.; Dimitrov, N.; Sieradzki, K. *Nature* **2001**, *410*, 450−453.

(48) Caldwell, K. M.; Ramaker, D. E.; Jia, Q.; Mukerjee, S.; Ziegelbauer, J. M.; Kukreja, R. S.; Kongkanand, A. *J. Phys. Chem. C* **2015**, *119*, 757−765.

(49) Neyerlin, K. C.; Srivastava, R.; Yu, C.; Strasser, P. *J. Power Sources* **2009**, *186*, 261−267.

(50) Teliska, M.; O'Grady, W. E.; Ramaker, D. E. *J. Phys. Chem. B* **2005**, *109*, 8076−8084.

(51) Mukerjee, S.; Srinivasan, S.; Soriaga, M. P.; McBreen, J. *J. Electrochem. Soc.* **1995**, *142*, 1409−1422.

(52) Wang, J. X.; Ma, C.; Choi, Y.; Su, D.; Zhu, Y.; Liu, P.; Si, R.; Vukmirovic, M. B.; Zhang, Y.; Adzic, R. R. *J. Am. Chem. Soc.* **2011**, *133*, 13551−13557.

(53) Dubau, L.; Asset, T.; Chattot, R.; Bonnaud, C.; Vanpeene, V.; Nelayah, J.; Maillard, F. *ACS Catal.* **2015**, *5*, 5333−5341.

(54) Lopez-Haro, M.; Dubau, L.; Guétaz, L.; Bayle-Guillemaud, P.; Chatenet, M.; André, J.; Caqué, N.; Rossinot, E.; Maillard, F. *Appl. Catal., B* **2014**, *152−153*, 300−308.

(55) Dubau, L.; Lopez-Haro, M.; Durst, J.; Guetaz, L.; Bayle-Guillemaud, P.; Chatenet, M.; Maillard, F. *J. Mater. Chem. A* **2014**, *2*, 18497−18507.

(56) Vegard, L. *Eur. Phys. J. A* **1921**, *5*, 17−26.

(57) Hwang, B.-J.; Sarma, L. S.; Chen, J.-M.; Chen, C.-H.; Shih, S.-C.; Wang, G.-R.; Liu, D.-G.; Lee, J.-F.; Tang, M.-T. *J. Am. Chem. Soc.* **2005**, *127*, 11140−11145.

(58) Norskov, J. K.; Bligaard, T.; Rossmeisl, J.; Christensen, C. H. *Nat. Chem.* **2009**, *1*, 37−46.

(59) Stamenkovic, V.; Mun, B. S.; Mayrhofer, K. J. J.; Ross, P. N.; Markovic, N. M.; Rossmeisl, J.; Greeley, J.; Nørskov, J. K. *Angew. Chem., Int. Ed.* **2006**, *45*, 2897−2901.

(60) Nesselberger, M.; Ashton, S.; Meier, J. C.; Katsounaros, I.; Mayrhofer, K. J. J.; Arenz, M. *J. Am. Chem. Soc.* **2011**, *133*, 17428−17433.

(61) Perez-Alonso, F. J.; McCarthy, D. N.; Nierhoff, A.; Hernandez-Fernandez, P.; Strebel, C.; Stephens, I. E. L.; Nielsen, J. H.; Chorkendorff, I. *Angew. Chem., Int. Ed.* **2012**, *51*, 4641−4643.

(62) Shao, M.; Peles, A.; Shoemaker, K. *Nano Lett.* **2011**, *11*, 3714−3719.

(63) Teliska, M.; O'Grady, W. E.; Ramaker, D. E. *J. Phys. Chem. B* **2004**, *108*, 2333−2344.

(64) Roth, C.; Benker, N.; Buhrmester, T.; Mazurek, M.; Loster, M.; Fuess, H.; Koningsberger, D. C.; Ramaker, D. E. *J. Am. Chem. Soc.* **2005**, *127*, 14607−14615.

(65) Conway, B. E. *Ionic hydration in chemistry and biophysics*; Elsevier/North-Holland: Amsterdam, New York, 1981.

(66) Erickson, E. M.; Thorum, M. S.; Vasić, R.; Marinković, N. S.; Frenkel, A. I.; Gewirth, A. A.; Nuzzo, R. G. *J. Am. Chem. Soc.* **2012**, *134*, 197−200.

(67) Stephens, I. E. L.; Bondarenko, A. S.; Gronbjerg, U.; Rossmeisl, J.; Chorkendorff, I. *Energy Environ. Sci.* **2012**, *5*, 6744−6762.

(68) Jia, Q.; Ramaswamy, N.; Hafiz, H.; Tylus, U.; Strickland, K.; Wu, G.; Barbiellini, B.; Bansil, A.; Holby, E. F.; Zelenay, P.; Mukerjee, S. *ACS Nano* **2015**, *9*, 12496−12505.